

One-Step Electrodeposition of Iron Oxyhydroxide Onto 3D Porous Graphene Substrates for on Chip Asymmetric Micro-Supercapacitors

Filipe Braga,^[a] Gabriel Casano,^[b] Manel Sonni,^[c] Harry Finch,^[d] Vinod R. Dhanak,^[a, e] Marco Caffio,^[b] and Laurence J. Hardwick^{*[a]}

Electrochemical capacitors based on redox active materials can achieve greater capacitance values than traditional electric double layer composites. Herein, electrodeposition of iron oxyhydroxide from a mildly acidic acetate precursor is reported. The one-step deposition resulted in a submicron film composed of FeOOH phase, which was confirmed via Raman and x-ray photoelectron spectroscopy. The capacitance increased linearly with loading amount and achieved a maximum at 1600 mC deposition with 120 mFCm^{-2} at 25 mVs^{-1} after which the film became more resistive, limiting electrolyte access to the porous graphene substrate. The deposited FeOOH demonstrated promising rate capability and good cycling stability, without

phase changes, retaining 82 % of the initial capacitance after 5000 consecutive charge/discharge cycles. The charge storage mechanism of FeOOH was determined via *in situ* Raman spectroscopy, which followed reversible iron oxygen vibration changes upon cycling which become more intense upon reduction as a result of sodium ion intercalation. Furthermore, an asymmetric configuration full cell combining FeOOH/MnO₂ allowed the working voltage to be extended to 2 V, maintaining an ideal capacitor behaviour, and achieving a maximum energy and power density of $21 \mu\text{Wh cm}^{-2}$ and 2.5 mW cm^{-2} respectively.

Introduction

Electrochemical capacitors are key components within electric mobility, portable electronics, and renewable energy supply applications.^[1] These devices are characterised by high-power density (fast-charging) and long cycle-life, requiring virtually no maintenance or replacement during application.^[2] On this account, electrochemical capacitors are being investigated for new applications in internet-of-things (IoT) networks, miniatur-

ised electronics, drug delivery and smart buildings, where autonomy is essential.^[3–5]

State-of-the art devices in industry use a combination of high-surface area carbon electrodes and organic electrolytes, due to their large operation window. Aqueous electrolytes have their commercial application hindered by the chemical stability of water (1.23 V), however are an attractive alternative due to potentially lower cost, safety, sustainability and higher ionic mobility.^[6] Polymer additives can form hydrogels which enable flexible on-chip microsupercapacitors.^[7]

To go beyond the limits of water-based electrolytes, an asymmetric configuration can be used in which distinct electrodes with balancing working voltages are connected. This arrangement typically uses pseudocapacitive compounds, where the charge is stored via fast and reversible faradaic electron transfer, thus mimicking the behaviour of traditional electric double-layer capacitors. As well as achieving higher capacitances, this configuration increases the overpotential on oxygen and hydrogen evolution effectively increasing the voltage window.^[8]

Metal oxides, such as RuO₂ and MnO₂, are common pseudocapacitive materials via rapid redox reactions at the interface and are typically used as the positive electrode in full cells.^[9–11] For the negative electrode, however, the best candidates are not evident due to the capacitance obtained being significantly lower than the positive electrode.^[12] Several materials with complementary voltage windows to manganese oxide can be combined in an asymmetric device, such as active carbons, conductive polymers and metal oxides.^[13–18] From the later, various iron oxides have been investigated as the negative electrode in asymmetric devices due to low associated costs,

[a] F. Braga, V. R. Dhanak, L. J. Hardwick
Stephenson Institute for Renewable Energy, Department of Chemistry,
University of Liverpool, Chadwick Building, Peach Street Liverpool, L69 7ZF
England, United Kingdom
E-mail: hardwick@liverpool.ac.uk

[b] G. Casano, M. Caffio
Integrated Graphene Ltd, Euro House, Stirling FK8 2DJ, Scotland, United Kingdom

[c] M. Sonni
Materials Innovation Factory, Department of Chemistry, University of Liverpool, 51 Oxford Street, Liverpool, L7 3NY England, United Kingdom

[d] H. Finch
Department of Electrical Engineering and Electronics, University of Liverpool, Liverpool L69 3GJ, England, United Kingdom

[e] V. R. Dhanak
Department of Physics, The University of Liverpool, Crown Street, Liverpool L69 7ZD, England, United Kingdom

 Supporting information for this article is available on the WWW under <https://doi.org/10.1002/batt.202400431>

 © 2024 The Authors. Batteries & Supercaps published by Wiley-VCH GmbH. This is an open access article under the terms of the Creative Commons Attribution License, which permits use, distribution and reproduction in any medium, provided the original work is properly cited.

large operational working voltage, environmentally benign – low toxicity and earthly abundance. The main challenges that need to be addressed are limited ionic diffusion and electric conductivity, which can result in capacitances much lower than the theoretical value, difficulties to charge balance with the positive electrode and poor rate capability.^[19]

Different iron oxide polymorphs have been studied for electrochemical capacitor applications in combination with carbon and polymer substrates to increase conductivity, such as magnetite Fe_3O_4 , hematite Fe_2O_3 , akageneite $\beta\text{-FeOOH}$ and lepidocrocite $\gamma\text{-FeOOH}$.^[20–25] From these, iron oxyhydroxide is a promising candidate due to high capacitance and operational voltage windows ranging from 0.8 to 1.2 V. Crystalline materials typically show a tunnel like structure that is ideal for fast redox reactions, like MnO_2 birnessite storage mechanism.^[26] Chen and co-workers have investigated their pseudocapacitive mechanism via *in situ* X-ray absorption near-edge structure (XANES) and found the intercalation of Li^+ charge carriers into 2D layered channels of FeO_6 octahedra as the storage mechanism. The expansion and contraction of the layered structure was matched with the oxidation variations in the metal centre.^[25]

Herein a new electrodeposition route to prepare FeOOH films with agglomerated nanoparticle structure using an iron (II) acetated solution is reported that enhances the performance when compared to traditional acidic deposition. The charge storage mechanism of the electrodeposited FeOOH was also examined via *in situ* Raman spectroscopy. The obtained iron oxyhydroxide was used as the negative electrode in aqueous electrochemical capacitors, achieving a capacitance of 120 mF/cm² at 25 mV/s and high retention of 82% after 5000 charge/discharge cycles. Furthermore, this material was combined with a birnessite MnO_2 acting as the positive electrode in asymmetric configuration allowing the voltage window to extend up to 2 V achieving whilst maintaining ideal capacitor behaviour and achieving high energy 21 $\mu\text{Wh cm}^{-2}$ and power density 2.5 mW cm⁻².

Experimental

FeOOH Electrodeposition Onto Porous Graphene

Electrodeposition was performed using a graphene foam (GF) electrode on polyimide substrates supplied by Integrated Graphene Ltd. A 30 mM solution of iron (II) acetate $\text{Fe}(\text{CH}_3\text{COO})_2$ (95%, Sigma Aldrich) was prepared for the deposition. Galvanostatic deposition was implemented using a constant current density of 1.25 mA/cm² with a charge cut-off varying from 0.4 to 2.4 C. Iron (III) chloride (97%, Sigma Aldrich) galvanostatic deposition was performed using a 3 mA current with a 15 C charge cut-off using a 50 mM solution. Iron (II) chloride (98%, Sigma Aldrich) potentiostatic deposition was performed using a 0.7 V vs Ag/AgCl potential for 3 hours using a 5 mM solution. After electrodeposition, the chip electrode was washed carefully with deionised water and oven dried for 2 hours at 60 °C.

Physicochemical Characterisation

The FeOOH surface morphology was analysed using a JEOL JSM-7001F FEGSEM operating at 20 kV acceleration voltage fitted with an energy dispersive X-ray spectroscopy (EDS) analysis equipment (Oxford Instruments ONCAx-act X-ray detector). The surface elemental analysis was performed via X-ray photoelectron spectroscopy measurements under ultra-high-vacuum ($\sim 10^{-10}$ mbar) conditions using a monochromated, aluminium x-ray source (1486.6 eV) operated at 150 W. The spectrometer was calibrated using the core levels (CLs) and Fermi energy of a clean silver foil and was operated with an overall resolution of ± 0.1 eV. Powder X-ray diffraction (PXRD) data were collected in Debye-Scherrer transmission geometry with sample powders loaded into 1.5 mm diameter borosilicate glass capillaries on a Rigaku SmartLab instrument equipped with a 9 kW rotating anode source providing a parallel beam of Mo K α radiation ($\lambda = 0.70930$ Å). Raman analysis was recorded with a 532 nm laser using a Raman system (Renishaw inVia Reflex) focused via 50x objective (Leica). Laser power varied between 0.2 to 2 mW. For *in situ* Raman microscopic analysis, an in-house cell was devised using a 3-D printed body that enabled contact with the electrode facing up the microscope lens.^[26] The cyclic voltammetry profile was recorded between 0 and -0.8 V vs Ag/AgCl at 0.5 mV/s in 5 M NaClO₄. Raman spectra were recorded with a 532 nm laser using a Raman system (Renishaw inVia Reflex) focused via 50x objective (Leica). To avoid laser damage, the estimated power was limited to 0.2 mW. A spectrum was collected every 60 mV during the charge/discharge process within a range of 200 – 900 cm⁻¹.

Electrochemical Characterisation

The electrochemical cell consisted of an electrodeposited FeOOH working electrode 0.06 cm² with 40 μm thickness, a graphene foam counter electrode 0.60 cm² and Ag/AgCl reference electrode. Measurements were performed using deaerated 5 M NaClO₄ electrolyte at 25 °C. Cyclic voltammograms (CVs) were recorded at varying scan rates 10 – 500 mV s⁻¹ and galvanostatic charge/discharge at varying current densities 0.5 – 20 mA cm⁻².

The capacitive behaviour of the GF-FeOOH electrodes was further investigated by potentiostatic electrochemical impedance spectroscopy (PEIS) in the 1 MHz to 10 mHz frequency range with 10 mV sinus amplitude around the open circuit potential. In full cell configuration, the negative electrode was the GF-FeOOH and the positive electrode was an optimised MnO_2 deposition which the synthesis is described in detail elsewhere.^[26] In short, a 100 mM solution of manganese (II) acetate tetrahydrate (99.99%, Sigma Aldrich) was used with current pulses of 1 s (2 mA) 'on' followed by 2 s (-0.8 mA) 'off' with a total 0.24 C charge cut off value.

The areal capacitance for a single electrode was calculated from GCD data according to equation 1, where $A_{\text{geometric}} = \text{working electrode area}$ and $EW = \text{maximum voltage set} - V_{\text{drop}}$. ESR was calculated from the GCD voltage drop by equation (2). Energy and power densities were obtained using equations 3 and 4 and normalised using the total areal of both electrodes. Energy and coulombic efficiencies were obtained using equations 5 and 6.

$$\text{Areal Electrode Capacitance} \left[\frac{\text{mF}}{\text{cm}^2} \right] = 2 * \frac{\int (I \text{ [A]} * V \text{ [V]}) dt \text{ [s]}}{A_{\text{geometric}} \text{ [cm}^2\text{]} * (EW)^2 \text{ [V}^2\text{]}} * 1000 \quad (1)$$

$$ESR_{\text{GCD}} [\Omega] = \frac{V_{\text{drop}} \text{ [V]}}{2 * \text{Input I} \text{ [A]}} \quad (2)$$

$$Energy [J] = \int (I [A]^* V [V]) dt [s] \quad (3)$$

$$Power [W] = E/\Delta t \quad (4)$$

$$Energy Efficiency [\%] = \frac{E_{\text{discharge}} [J]}{E_{\text{charge}} [J]} * 100 \quad (5)$$

$$Coulombic Efficiency [\%] = \frac{C_{\text{discharge}} [C]}{C_{\text{charge}} [C]} * 100 \quad (6)$$

Results and Discussion

Characterisation of FeOOH Electrodeposition

FeOOH can be obtained via iron (III) chloride hydrolysis or via acidic electrooxidation of iron (II) precursor, such as ferrous chloride and ferrous sulphate, where Fe^{2+} ions are oxidised at $E_0=0.77$ V vs SHE to Fe^{3+} , followed by the precipitation of iron oxyhydroxide due to limited solubility.^[19,27,28] An electrodeposition procedure following the same mechanism is developed here, however a weaker acidic iron acetate precursor is used.

Lowering the acidity of the solution facilitates the oxidation of ferrous ion and reduces the solubility of the iron oxyhydroxide, seen both on the lower potential for the oxidation and on the irreversible cyclic voltammetry profile in the acetate precursor (Figure S1).

The resulting product of the one-step electrooxidation of iron acetate precursors was investigated via XPS, Figure 1. The full survey spectrum shows the existence of Fe, O and C elements on the electrode. The Fe 2p spectra shows a distinct peak at 711 eV for $\text{Fe} 2p_{1/2}$, followed by a peak at 725 eV for $\text{Fe} 2p_{3/2}$. Two satellite peaks are seen at 732 eV and 718 eV which have been described previously for Fe^{3+} in FeOOH compounds and differentiate from the spectra of other phases such as hematite and magnetite.^[29–31] The O 1s spectra also shows two main distinct peaks associated with $\text{Fe}-\text{O}-\text{H}$ and $\text{Fe}-\text{O}-\text{Fe}$ bonds and a weak shoulder peak can also be fitted associated with adsorbed water. Deconvolution of the C 1s core level spectrum shows a strong peak at 285 eV from the porous graphene substrate with smaller peaks at higher binding energy associated with oxygenated groups. The XPS data is in good agreement with other literature reports and indicates the successful synthesis of FeOOH/graphene composites via iron (II)

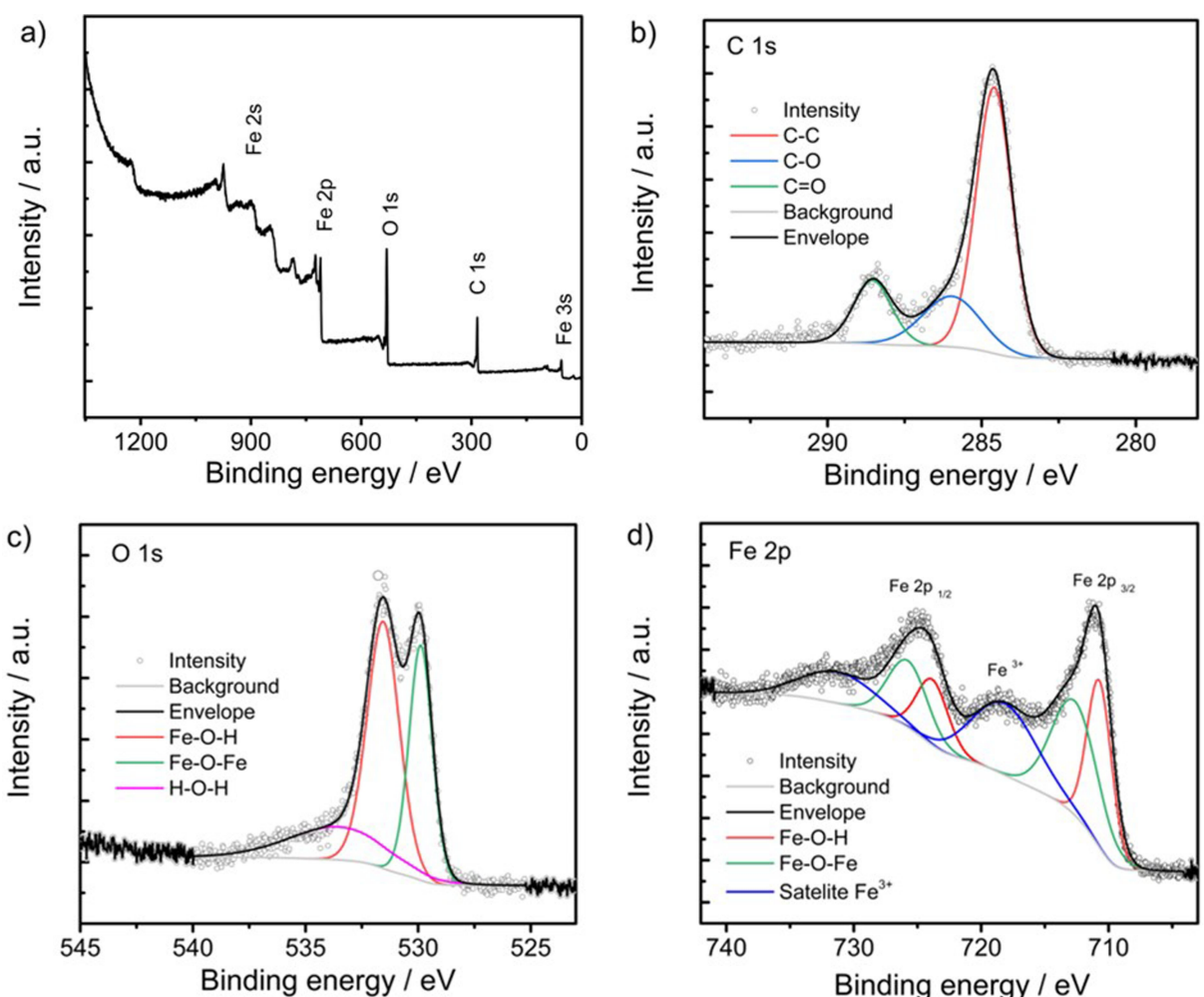


Figure 1. a) X-ray photoelectron spectroscopy survey spectrum, b) C 1s core level spectrum, c) O 1s core level spectrum and d) Fe 2p core level spectrum of graphene-foam electrode with iron oxyhydroxide deposit (GF-FeOOH-1600 mC).

acetate precursors and it differs from previous electrodeposition procedures which obtain a hydrated form of FeOOH.^[25,30,32]

The PXRD pattern of the electrodeposited GF-FeOOH-1600 mC electrode can be seen in Figure S2. Reflections for graphite with poor crystallinity are clearly observed on the sample with only a few additional peaks. This is attributed to a relative low loading of FeOOH on the carbon substrate and low crystallinity, which is common in samples prepared via electrodeposition.^[33-34] The main peak of lepidocrocite, one of the polymorphs of FeOOH, overlaps with the prominent peaks of graphite, making it challenging assign the FeOOH structure using PXRD alone.

To further determine the phase of the electrodeposited iron oxide, Raman analysis was conducted shown in Figure 2 for the GF-FeOOH-1600 mC electrode, which is representative of the other cut-off charges. Four characteristic bands for FeOOH are observed at 325, 415, 537 and 725 cm⁻¹ in good agreement with the literature.^[35-39] The broad features observed are indicative of a low crystallinity deposit. The two bands at 325 cm⁻¹ and 415 cm⁻¹ are associated with symmetric Fe–O vibration modes in different octahedral sites and the bands at 537 cm⁻¹ and 725 cm⁻¹ are described as asymmetric bending modes of Fe–O. This further corroborates the XPS characterisation. Furthermore, when increasing the laser power, Figure S3, the local heating from the Raman microscope causes a phase transition from iron oxyhydroxide to hematite (Fe₂O₃), which is a well known thermal degradation process for FeOOH.^[28,39]

The morphology of the graphene foam working electrodes after the deposition procedure was systematically analysed via SEM (Figure 3) for the different cut-off charges and its chemical composition via EDS, Figure S4. At lower loadings, a roughening of the carbon surface can be seen at high magnification

(Figure 3d) compared to the pristine graphene images. At 800 mC FeOOH, distinguishable nanoparticles are seen formed at the edges of the carbon porous structure. In the GF-FeOOH-1600 mC electrode (Figures 3g,h), the agglomerated particles increase significantly in while the porous network of the graphene is maintained, which is essential to avoid pore blockage. This is especially important when using metal oxide pseudocapacitors, which are known to suffer from limited conductivity. At higher magnification, the FeOOH particles are highly agglomerated spherical particles ranging from 300–500 nm. This type of electrode structure is consistent with other electrodeposited FeOOH in aqueous media.^[33] Upon further electrodeposition for the 2400 mC charge cut-off (Figures 3i,j), the film thickness increases considerably pore blockage is seen via interfacial saturation and growth of the nanoparticles.

Electrochemical Performance of Graphene-FeOOH Electrodes

Initial electrochemical characterisation of the FeOOH electrode was performed to understand their respective capacitances and stable working window (Figure 4). Due to poor electronic conductivity characteristic of FeOOH, it is important to optimise the electrodeposition parameters and electrode thickness. CV measurements (Figure 4a) show typical pseudocapacitive shape for iron oxides with a linear increase in current response from 400 to 1600 mC deposition charge and a maximum capacitance was achieved of 120 mF cm⁻² at 25 mV s⁻¹ and 160 mF cm⁻² at 0.5 mA cm⁻². Further increase in the loading amount caused the CV shape to deviate from a capacitive response and the current to decrease due to diffusion limitations in the electrode. Electrochemical impedance spectroscopy analysis shows a bode plot with phase angles close to 90 degrees at the low frequency

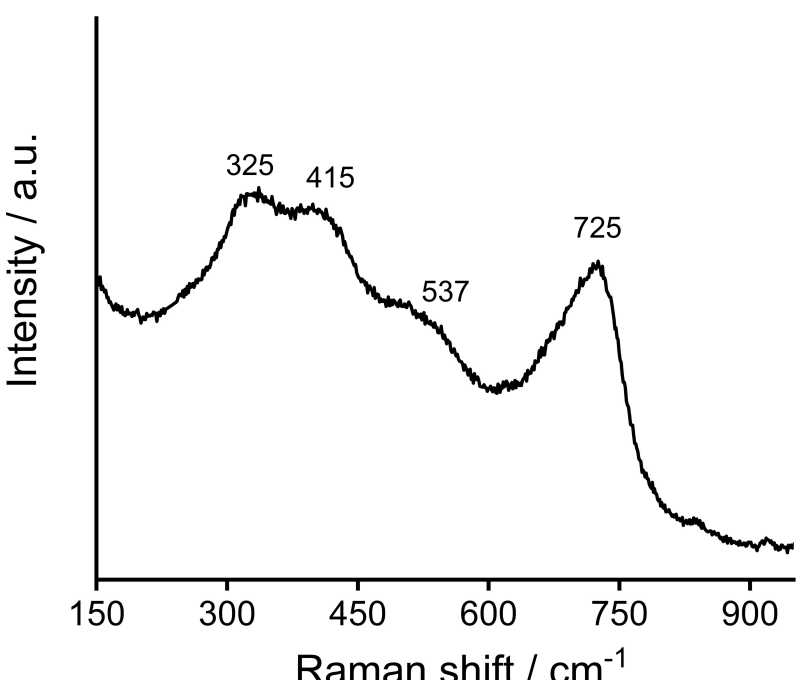


Figure 2. Raman spectrum of graphene-foam electrode with iron oxyhydroxide deposit (GF-FeOOH-1600 mC).

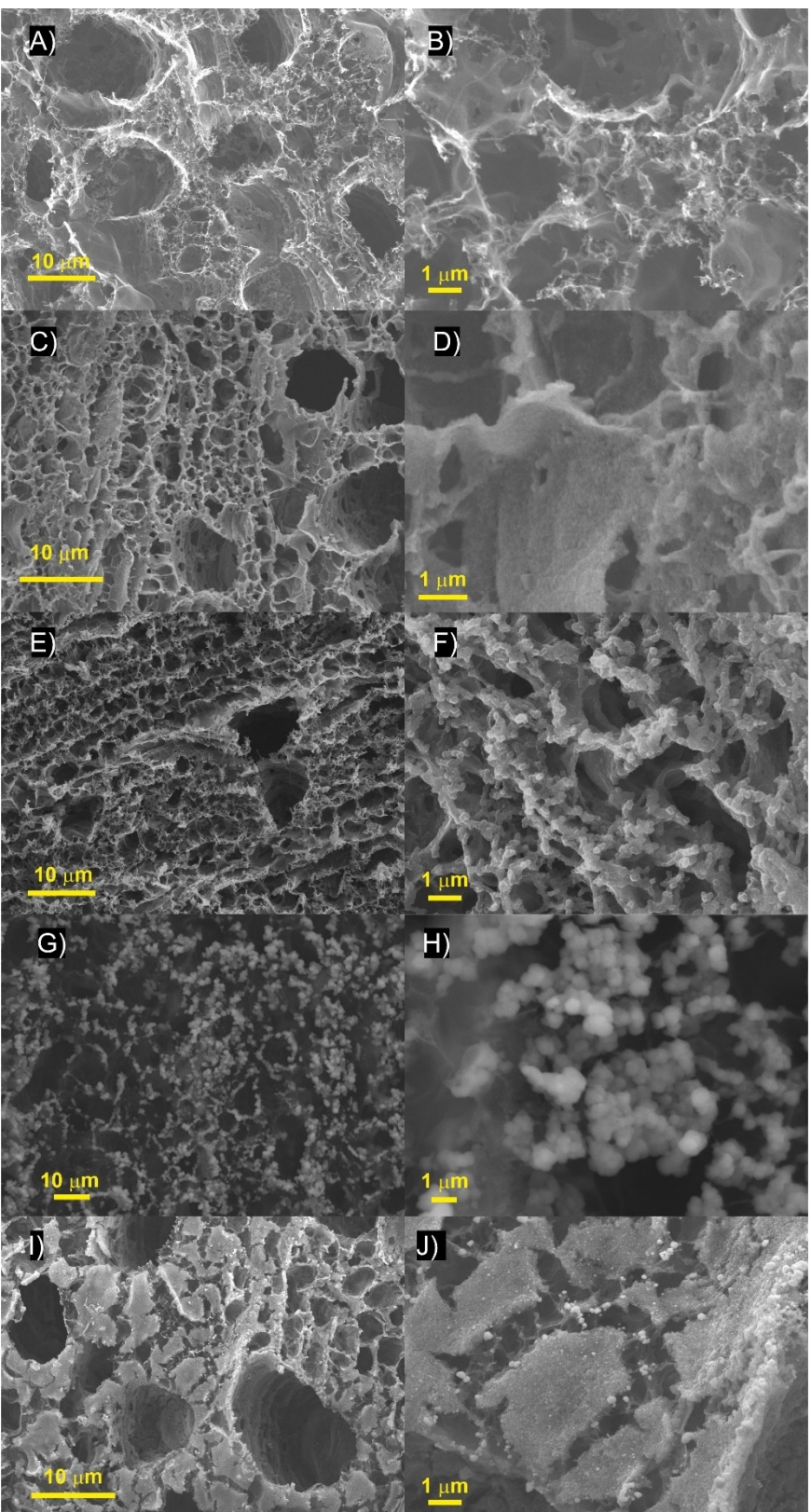


Figure 3. SEM analysis of a,b) pristine graphene-foam and iron oxyhydroxide electrodeposition with different charge cut-off, c,d) GF-FeOOH-400 mC, e,f) GF-FeOOH-800 mC, g,h) GF-FeOOH-1600 mC and i,j) GF-FeOOH-2400 mC at low (left) and high (right) magnifications.

region indicating capacitive behaviour. The time constant values obtained at 45° phase angle increase with the thickness

of the FeOOH electrode without inflection point. However, the time constant at GF-FeOOH-2400, 1.8 s, mC is not signifi-

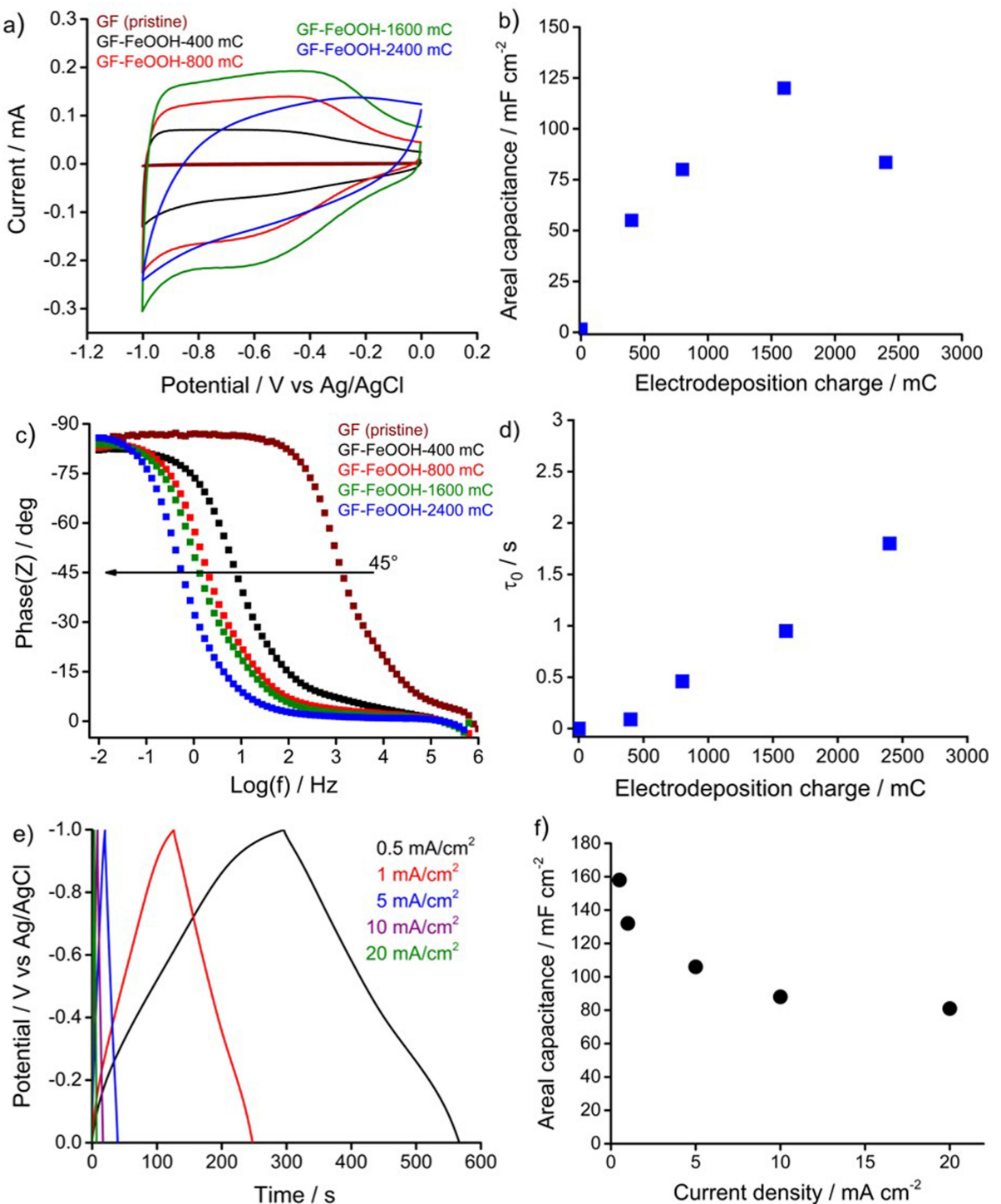


Figure 4. a) CV curves at 25 mVs^{-1} , b) capacitance vs electrodeposition charge plots, c) Electrochemical Impedance Spectroscopy (EIS) Bode plots, d) time constant vs electrodeposition charge plots of GF-FeOOH electrodes in 5 M NaClO_4 , e) galvanostatic charge/ discharge (GCD) curves at 0.5 to 20 mA cm^{-2} and f) areal capacitance vs current density of GF-FeOOH-1600 mC in 5 M NaClO_4 .

cantly high for faradaic materials (Figure 4d), which suggests that the capacitance decay is due to poor utilisation of the electroactive surface area due to the increase in film thickness seen in Figures 3i,j. The FeOOH film also shows good rate capability from 0.5 to 20 mA cm^{-2} with reasonable capacitance values at high rates. The GF-FeOOH optimised electrode

obtained from an iron acetate solution and traditional iron (II) and iron (III) chloride are compared in Figure S5. The novel synthetic route results in higher areal capacitances and lower equivalent series resistance when tested in the same galvanostatic charge/discharge conditions, thus highlighting the improvements in increasing the pH of the electrodeposition bath.

The rate capability of the optimised FeOOH electrode was further analysed via cyclic voltammetry at varying scan rates, Figure S6. The system starts to deviate from the ideal capacitive behaviour up to 500 mVs^{-1} , which indicates faster kinetics compared to similar FeOOH electrodeposited materials.^[33,34] The scan rate (v) dependent current is composed of diffusion and surface limited components that can be described by a simplification of the Cottrell equation $i = av^b$ where a is a constant related to electrode area, $\text{Fe}^{2+/\text{3}+}$ redox centres concentration and diffusion constant for charge transfer; i is the current and b contains information on whether the voltammetric processes are diffusion or surface limited.^[40,41] After plotting $\log v$ vs $\log i$, the slope of the straight line was found to be ≈ 1 (0.9), which indicates that the capacitive behaviour is predominantly governed by surface processes such as charge transfer at $\text{Fe}^{2+}/\text{Fe}^{3+}$ centres, consistent with similar FeOOH/carbon composites previously reported.^[42]

The precise origin of the pseudocapacitance mechanism of iron oxide/hydroxide are not fully understood, particularly for electrodeposited FeOOH onto carbon composites, which tend to have low long-range ordering. Here, *in situ* Raman microscopy was used to study the charge storage of the FeOOH electrode under potential control, Figure 5. After cell assembly, the spectrum at open circuit potential (OCP) shows the main iron-oxygen vibration mode becomes slightly broader and with

lower intensity compared to the pristine electrode as the electrolyte bands dominate, Figure S7. Band broadening can be explained by a hydration effect also observed in other transition metal oxides.^[26,43] The electrolyte bands at 630 and 465 cm^{-1} associated with the perchlorate ion remain unchanged throughout the charge/discharge process.^[44] As the electrode is discharged towards negative potentials, the peak at 680 cm^{-1} progressively increases in intensity and as the electrode is cycled back to zero volts, the intensity gradually decreases, similar to the initial stage after oxidation with a shoulder peak at 720 cm^{-1} .

The reversibility of the Raman bands confirms the high electronic and ionic conductivity of the graphene/FeOOH electrode which accounts for the high capacitance iron redox processes and highlights the charge storage results in the alteration of the Fe–O bonding in the material. Chen and co-workers investigated the charge storage mechanism of FeOOH electrodes within Li_2SO_4 (aq) via *in situ* X-ray absorption spectroscopy (XAS) and reported that the interatomic Fe–O bond distance increases with the $\text{Fe}^{3+}/\text{Fe}^{2+}$ reduction at -0.8 V vs Ag/AgCl.^[25] As the Fe–O bond distance increases in octahedral units, the Raman vibration mode becomes more polarisable and the intensity achieves its maximum at negative potential as an effect of the sodium intercalation which compensates the redox transition to larger Fe^{2+} ionic radii.

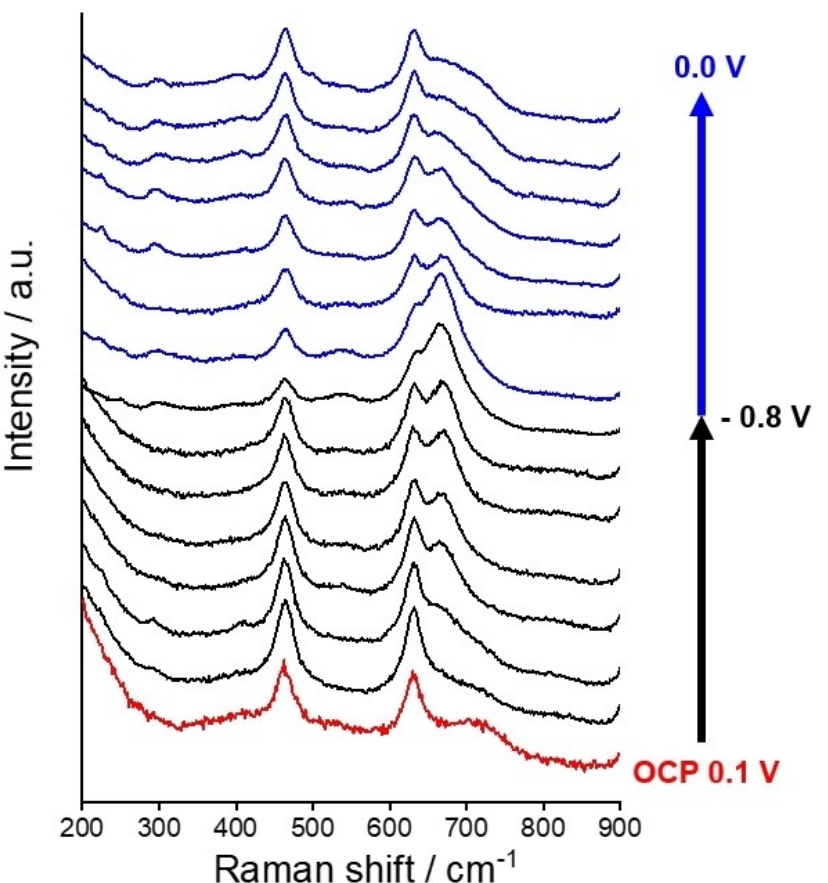


Figure 5. *In situ* Raman microscopy on the initial charge/discharge cycle of GF-FeOOH-1600-mC curing cyclic voltammetry at 0.5 mV/s in 5 M NaClO_4 electrolyte.

These results confirm the charge storage mechanism of the FeOOH electrode via reversible intercalation of the sodium ions, Equation 7.



The stability of the optimised GF-FeOOH electrode was tested via galvanostatic cycling at 10 mA cm^{-2} in sodium perchlorate electrolyte (Figure 6a). After an initial capacitance decay, the cycling profile remain steady and an 82% retention is obtained after 5000 consecutive cycles showing good performance compared to similar FeOOH/carbon electrodes on the literature. Raman characterisation (Figure 6b) of the electrode at the end of the cycling procedure shows that no phase change is observed as the same bands related to symmetric and asymmetric vibrations on the FeO_6 octahedra are obtained (described in Table 1). Deconvolution of the main peak Fe-O vibration peak at 725 cm^{-1} shows a broader envelope after cycling, with a shoulder feature at 680 cm^{-1} which is the same peak position of the Fe-O bond vibration in the sodiated FeOOH seen on the *in situ* Raman data (Figure 5) for the fully discharged electrode, $\text{NaFe(II)}\text{OOH}$. This analysis further corroborates the intercalation/deintercalation storage mechanism of FeOOH and suggests a degree of irreversible intercalation of sodium ions after 5000 charge/discharge cycles that accounts for the capacitance loss as it hinders the $\text{Fe}^{3+}/\text{Fe}^{2+}$ faradaic reactions as well as deteriorating mechanical stability. Further-

more, iron dissolution into the electrolyte upon the oxidation/reduction of the electrode has also been reported on the literature as cause for capacitance fade, however, in this study this was not evident.^[32,45]

Asymmetric FeOOH// MnO_2 Capacitor

After FeOOH was electrochemically characterised in the electrolyte of choice, an asymmetric device was assembled in combination with a birnessite MnO_2 positive electrode. The optimisation of electrodeposited MnO_2 has been described elsewhere, however it undergoes a similar process of the capacitance being directly related to the loading amount, which allows the charge balance between both electrodes that is essential in asymmetric configuration (Figure S6). The voltage of the full cell device was extended from 1.4 to 2.0 V, Figure S9, and maintained the ideal capacitor behaviour with symmetric curves on both cyclic voltammetry and GCD experiments. Figure 7 shows the electrochemical performance of the full cell at 2 V showing that the ideal capacitor behaviour is maintained when enlarging the voltage window as well as varying scan rate and current density. The full cell has high coulombic efficiency (CE) and low equivalent series resistance (ESR) values at different rates. The energy efficiency (EE) is in line with pseudocapacitive materials which tends to be lower than classic activated carbon double layer capacitors. The performance of

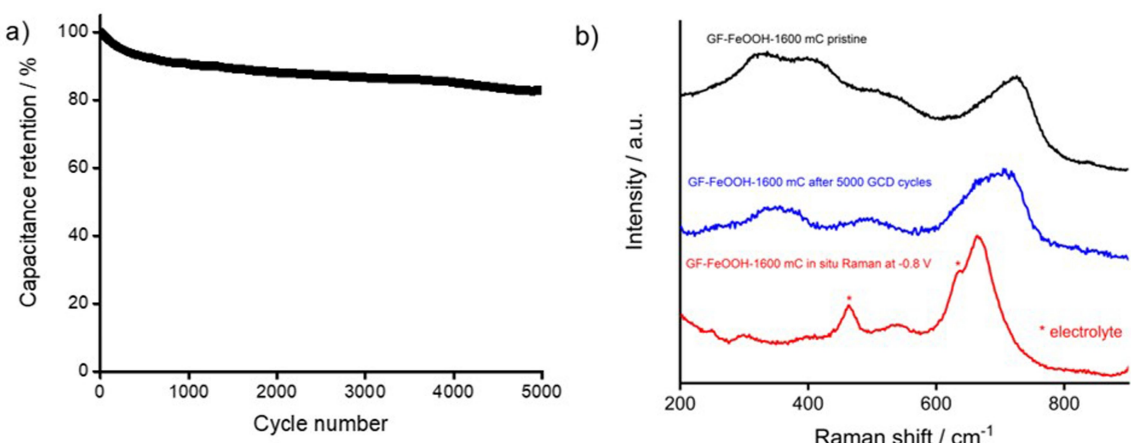


Figure 6. a) Cycling data via galvanostatic charge/discharge (GCD) at 10 mA cm^{-2} for GF-FeOOH-1600 mC in 5 M NaClO_4 and b) Raman spectra of the pristine GF-FeOOH-1600 mC electrode (black trace), after 5000 cycles (blue trace) and fully sodiated FeOOH from *in situ* Raman spectrum at -0.8 V taken from Figure 5 (red trace).

Table 1. Fitted Raman band positions and full width at half-maximum (FWHM) of FeOOH. Bands are assigned according to the literature.^[35–39]

GF-FeOOH-1600 mC	Position (FWHM) (cm ⁻¹)	Band	Vibrational mode description
725 (75)		ν_1	Asymmetric $\text{Fe}-\text{OH}$ bending mode
537 (18)		ν_2	Asymmetric $\text{Fe}-\text{OH}$ bending mode
415 (23)		ν_3	Symmetric $\text{Fe}-\text{O}$ stretching vibration of FeO_6 octahedra
325 (36)		ν_4	Symmetric $\text{Fe}-\text{O}$ stretching vibration of FeO_6 octahedra

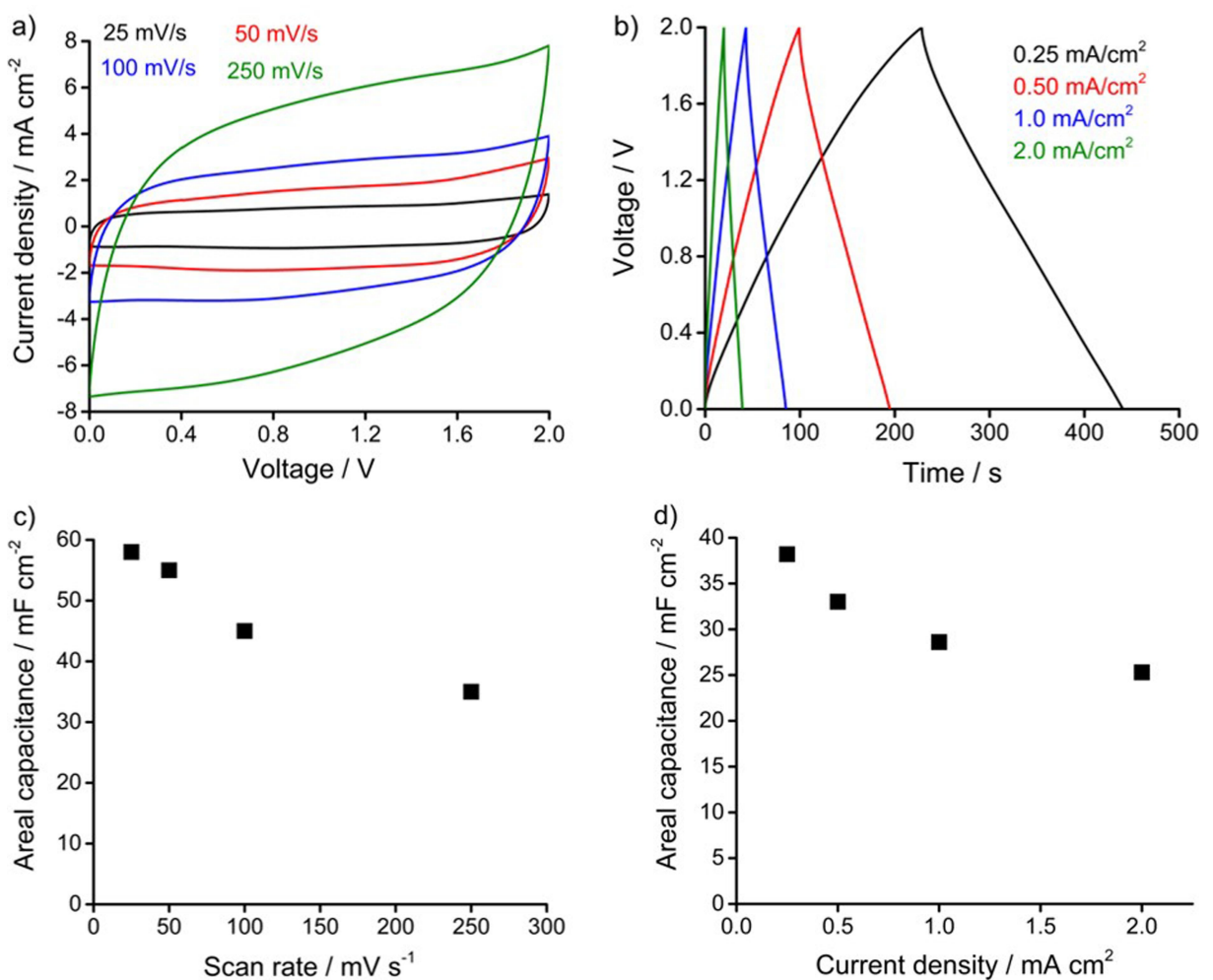


Figure 7. Electrochemical performance of GF-FeOOH//GF-MnO₂ full cell in CV a) and b) GCD and the areal capacitance plots versus c) scan rate from 25–250 mV s⁻¹ and d) current density from 0.25–2.0 mA cm⁻² in 5 M NaClO₄ electrolyte.

the full cell device at different current loadings is reported in Table 2. For the GF-FeOOH//GF-MnO₂ cell, the highest energy density achieved was 21 µWh cm⁻² (at 0.25 mA/cm²) and a power density of 2.5 mW cm⁻² at (2 mA/cm²). Table S1 compares similar full cell aqueous micro-supercapacitor devices in asymmetric configuration. The full range of energy and power densities is reported in Figure S10. Wang and co-workers report a device with volumetric capacitance of 1.1 F/cm³ at 20 mA/cm³ current density which results in an energy density of 0.48 mWh/cm³, while the current work obtained a volumetric capacitance of 9.5 F/cm³ and 5.3 mWh/cm³ at 62 mA/cm³.^[33] This is despite

the fact that the single electrode capacitance reported by Wang and co-workers is higher for the same current density. Li and co-workers obtained a maximum areal capacitance of 21.9 mF/cm² and energy density of 9.6 µWh/cm², while the current work achieved 33 mF/cm² and 18.3 µWh/cm² for the same 0.5 mA/cm² current density.^[18] Zhao et al. described an aqueous asymmetric MnO₂ vs Fe₂O₃ capacitor with 4.92 F/cm³ volumetric capacitance and 2.66 mWh/cm³ energy density at a power density of 19.72 mW/cm³, while for the same 2.0 mA/cm² current density and voltage window the GF-MnO₂-FeOOH-GF device displays 6.2 F/cm³ and 3.47 mWh/cm³ at a power density

Table 2. Full cell capacitive performance calculated from galvanostatic cycling data.

j (mA/cm ²)	Areal capacitance (mF/cm ²)	Volumetric capacitance (F/cm ³)	CE (%)	EE (%)	ESR (Ω)
0.25	38	9.5	95	71	0.7
0.5	33	8.2	97	75	0.8
1.0	29	7.2	99	78	0.9
2.0	25	6.2	99	80	0.9

of 625 mW/cm^3 .^[46] These values are highly dependent on the type of electrolyte and voltage window obtained and often report on a performance trade-off between energy and power density.

The full cell asymmetric device was tested for 5000 galvanostatic charge/discharge cycled and retained 70% of its initial capacitance (Figure 8). Analysis of the voltage split between the positive and negative electrode indicate that in the first cycle, the cell is charge balanced and each individual electrode remains in the stable window to avoid metal dissolution and phase transitions. Upon cycling, due to a different rate of degradation from the manganese and iron electrodes (Figure S11), this potential split becomes uneven and the iron oxyhydroxide starts to degrade more rapidly into the electrolyte at higher voltages. Thereby the future challenge in these types of devices is to overcome the differential rate at which the negative and positive electrodes retain capacitance, causing the cell to become charge unbalanced at the end of the cycle life.

Conclusions

Electrodeposition of iron oxyhydroxide (FeOOH) onto carbon substrates based on acetate precursors was demonstrated. The FeOOH phase was confirmed via Raman and XPS analysis while the morphology was characterised via SEM and EDS. This electrode outperformed the more established iron chloride deposition, due to a higher pH of the deposition bath and a more irreversible oxidation/precipitation of the iron (II) in solution. As the negative electrode material for aqueous electrochemical capacitor, the FeOOH optimised deposition displays promising performance with high areal capacitance compared to typical iron oxide electrodes, with 120 mF cm^{-2} at 25 mVs^{-1} cyclic voltammetry and high cycling stability at 82% retention after 5000 galvanostatic charge/discharge cycles. The capacitance limitation with higher loadings was found to be related to pore blocking at the graphene substrate due to high thickness, instead of increased resistance of the film. The capacitive storage mechanism of FeOOH was investigated via *in situ* Raman microscopy during operando conditions, following the evolution of the iron oxygen vibration mode during discharge because of the sodium insertion. Finally, an asymmetric device using a Birnessite MnO_2 positive electrode was assembled achieving a maximum energy density of $21 \mu\text{Wh cm}^{-2}$ and power density of 2.5 mW cm^{-2} as well as high charge efficiency and low resistance. The cycling stability of the full cell is reasonable at 70% retention after 5000 cycles and our findings indicate that a gradual unbalancing on the positive and negative electrode is responsible for the capacitance decay.

Acknowledgements

The authors gratefully acknowledge funding from the Innovate UK grant: G-Cap supercapacitor in All-Terrain Vehicles (G-CAP) (TS/S023518/1) for funding for the project as well Impact

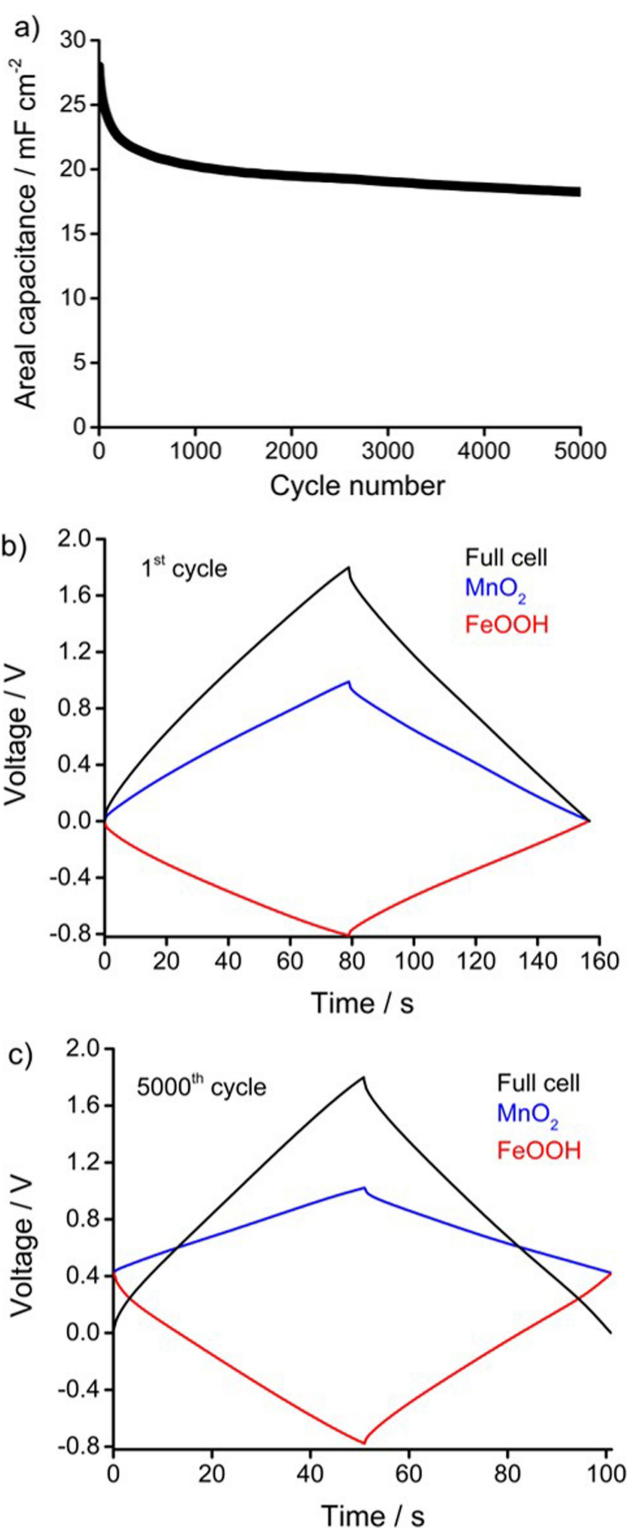


Figure 8. a) GCD at 1 mA cm^{-2} cycling data for GF-FeOOH// MnO_2 full cell at 1.8 V window in 5 M NaClO_4 and voltage split for the positive and negative electrodes on b) first and c) 5000^{th} cycle.

Accelerator Account Funding from the Engineering and Physical Sciences Research Council (EPSRC). The authors acknowledge the Imaging Centre at Liverpool for SEM access and Dr Matthew Bilton for the help with analysis and discussion.

Conflict of Interests

The authors declare no conflict of interest.

Data Availability Statement

The data that support the findings of this study are available from the corresponding author upon reasonable request.

Keywords: Pseudocapacitor · *In situ* Raman · Iron oxide · Asymmetric devices

- [1] P. Simon, Y. Gogotsi, *Nat. Mater.* **2020**, *19*(11), 1151–1163, <https://doi.org/10.1038/s41563-020-0747-z>.
- [2] J. R. Miller, A. Burke, *Electrochem. Soc. Interface* **2008**, *17*(1), 53, <https://doi.org/10.1149/2.f08081if>.
- [3] C. Lethien, J. Le Bideau, T. Brousse, *Energy Environ. Sci.* **2019**, *12*(1), 96–115, <https://doi.org/10.1039/C8EE02029A>.
- [4] X. Pan, X. Hong, L. Xu, Y. Li, M. Yan, L. Mai, *Nano Today* **2019**, *28*, 100764, <https://doi.org/10.1016/j.nantod.2019.100764>.
- [5] B. Bounor, B. Asbani, C. Douard, F. Favier, T. Brousse, C. Lethien, *Energy Storage Mater.* **2021**, *38*, 520–527, <https://doi.org/10.1016/j.ensm.2021.03.034>.
- [6] X. Zang, C. Shen, M. Sanghadasa, L. Lin, *ChemElectroChem* **2019**, *6*(4), 976–988, <https://doi.org/10.1002/celc.201801225>.
- [7] R. Jia, G. Shen, F. Qu, D. Chen, *Energy Storage Mater.* **2020**, *27*, 169–186, <https://doi.org/10.1016/j.ensm.2020.01.030>.
- [8] J. W. Long, D. Bélanger, T. Brousse, W. Sugimoto, M. B. Sassin, O. Crosnier, *MRS Bull.* **2011**, *36*(7), 513–522, <https://doi.org/10.1557/mrs.2011.137>.
- [9] Q. Jiang, N. Kurra, M. Alhabeb, Y. Gogotsi, H. N. Alshareef, *Adv. Energy Mater.* **2018**, *8*(13), 1703043, <https://doi.org/10.1002/aenm.201703043>.
- [10] H. Gao, F. Xiao, C. B. Ching, H. Duan, *ACS Appl. Mater. Interfaces* **2012**, *4*(5), 2801–2810, <https://doi.org/10.1021/am300455d>.
- [11] T.-H. Wu, Y.-H. Chu, C.-C. Hu, L. J. Hardwick, *Electrochem. Commun.* **2013**, *27*, 81–84, <https://doi.org/10.1016/j.elecom.2012.10.033>.
- [12] Q. Qu, S. Yang, X. Feng, *Adv. Mater.* **2011**, *23*(46), 5574–5580, <https://doi.org/10.1002/adma.201103042>.
- [13] V. Khomenko, E. Raymundo-Pinero, F. Béguin, *J. Power Sources* **2006**, *153*(1), 183–190, <https://doi.org/10.1016/j.jpowsour.2005.03.210>.
- [14] Y.-J. Peng, T.-H. Wu, C.-T. Hsu, S.-M. Li, M.-G. Chen, C.-C. Hu, *J. Power Sources* **2014**, *272*, 970–978, <https://doi.org/10.1016/j.jpowsour.2014.09.022>.
- [15] D. Liu, X. Wang, X. Wang, W. Tian, J. Liu, C. Zhi, D. He, Y. Bando, D. Golberg, *J. Mater. Chem. A* **2013**, *1*(6), 1952–1955, <https://doi.org/10.1039/C2TA01035F>.
- [16] M.-S. Wu, R.-H. Lee, *J. Electrochem. Soc.* **2009**, *156*(9), A737, DOI: 10.1149/1.3160547.
- [17] F.-L. Zheng, G.-R. Li, Y.-N. Ou, Z.-L. Wang, C.-Y. Su, Y.-X. Tong, *Chem. Commun.* **2010**, *46*(27), 5021–5023, <https://doi.org/10.1039/C002126A>.
- [18] L. Li, J. Zhang, Z. Peng, Y. Li, C. Gao, Y. Ji, R. Ye, N. D. Kim, Q. Zhong, Y. Yang, *Adv. Mater. (Deerfield Beach, Fla.)* **2015**, *28*(5), 838–845, <https://doi.org/10.1002/adma.201503333>.
- [19] B. Xu, M. Zheng, H. Tang, Z. Chen, Y. Chi, L. Wang, L. Zhang, Y. Chen, H. Pang, *Nanotechnology* **2019**, *30*(20), 204002, <https://doi.org/10.1088/1361-6528/ab009f>.
- [20] M. Navvar, R. Poon, R. Chen, R. P. Sahu, I. K. Puri, I. Zhitomirsky, *Carbon Energy* **2019**, *1*(1), 124–133, <https://doi.org/10.1002/cey2.6>.
- [21] C. Guan, J. Liu, Y. Wang, L. Mao, Z. Fan, Z. Shen, H. Zhang, J. Wang, *ACS Nano* **2015**, *9*(5), 5198–5207, <https://doi.org/10.1021/acsnano.5b00582>.
- [22] S. Shivakumara, T. R. Penki, N. Munichandraiah, *J. Solid State Electrochem.* **2014**, *18*, 1057–1066, <https://doi.org/10.1007/s10008-013-2355-1>.
- [23] M. Gaire, N. Khatoon, B. Subedi, D. Chrisey, *J. Mater. Res.* **2021**, *36*, 4536–4546, <https://doi.org/10.1557/s43578-021-00346-8>.
- [24] S. W. Bokhari, H. Pan, A. H. Siddique, M. Imtiaz, Z. Chen, Y. Li, S. Zhu, *Mater. Lett.* **2018**, *220*, 140–143, <https://doi.org/10.1016/j.matlet.2018.02.131>.
- [25] Y. C. Chen, Y. G. Lin, Y. K. Hsu, S. C. Yen, K. H. Chen, L. C. Chen, *Small* **2014**, *10*(18), 3803–3810, <https://doi.org/10.1002/smll.201400597>.
- [26] F. Braga, G. Casano, L. M. Daniels, M. Caffio, L. J. Hardwick, *Electrochim. Acta* **2023**, *455*, 142433, <https://doi.org/10.1016/j.electacta.2023.142433>.
- [27] Y. Zeng, M. Yu, Y. Meng, P. Fang, X. Lu, Y. Tong, *Adv. Energy Mater.* **2016**, *6*(24), 1601053, <https://doi.org/10.1002/aenm.201601053>.
- [28] R. L. Spray, K.-S. Choi, *Chem. Mater.* **2009**, *21*(15), 3701–3709, <https://doi.org/10.1021/cm803099k>.
- [29] H. Abdel-Samad, P. R. Watson, *Appl. Surf. Sci.* **1998**, *136*(1–2), 46–54, [https://doi.org/10.1016/S0169-4332\(98\)00337-7](https://doi.org/10.1016/S0169-4332(98)00337-7).
- [30] N. McIntyre, D. Zetaruk, *Anal. Chem.* **1977**, *49*(11), 1521–1529, <https://doi.org/10.1021/ac50019a016>.
- [31] L. Martinez, D. Leinen, F. Martin, M. Gabas, J. Ramos-Barrado, E. Quagliati, E. Dalchiele, *J. Electrochem. Soc.* **2007**, *154*(3), D126, <https://doi.org/10.1149/1.2424416>.
- [32] J. Liu, M. Zheng, X. Shi, H. Zeng, H. Xia, *Adv. Funct. Mater.* **2016**, *26*(6), 919–930, <https://doi.org/10.1002/adfm.201504019>.
- [33] F. Wang, Y. Zeng, D. Zheng, C. Li, P. Liu, X. Lu, Y. Tong, *Carbon* **2016**, *103*, 56–62, <https://doi.org/10.1016/j.carbon.2016.02.088>.
- [34] X. Gong, S. Li, P. S. Lee, *Nanoscale* **2017**, *9*(30), 10794–10801, <https://doi.org/10.1039/C7NR02896B>.
- [35] L. Wang, L. Deligniere, S. Husmann, R. Leiner, C. Bahr, S. Zhang, C. Dun, M. M. Montemore, M. Gallei, J. J. Urban, *Nano Res.* **2023**, *16*(7), 9352–9363, <https://doi.org/10.1007/s12274-023-5569-2>.
- [36] M. Szybowicz, M. Koralewski, J. Karoń, L. Melnikova, *Acta Phys. Pol. A* **2015**, *127*(2), 534–536, <https://doi.org/10.12693/aphyspola.127.534>.
- [37] W. R. Richmond, J. G. Hockridge, M. Loan, G. M. Parkinson, *Chem. Mater.* **2004**, *16*(17), 3203–3205, <https://doi.org/10.1002/chin.200442022>.
- [38] O. Zandi, A. R. Schon, H. Hajibabaei, T. W. Hamann, *Chem. Mater.* **2016**, *28*(3), 765–771, <https://doi.org/10.1021/acs.chemmater.5b03707>.
- [39] D. L. De Faria, S. Venâncio Silva, M. T. de Oliveira, J. Raman Spectrosc. **1997**, *28*(11), 873–878, [https://doi.org/10.1002/\(sici\)1097-4555\(199711\)-28:11%3C873::aid-jrs177%3E3.3.co;2-2](https://doi.org/10.1002/(sici)1097-4555(199711)-28:11%3C873::aid-jrs177%3E3.3.co;2-2).
- [40] K. Brezesinski, J. Wang, J. Haetge, C. Reitz, S. O. Steinmueller, S. H. Tolbert, B. M. Smarsly, B. Dunn, T. Brezesinski, *J. Am. Chem. Soc.* **2010**, *132*(20), 6982–6990, <https://doi.org/10.1021/ja9106385>.
- [41] W. Yan, J. Y. Kim, W. Xing, K. C. Donavan, T. Ayvazian, R. M. Penner, *Chem. Mater.* **2012**, *24*(12), 2382–2390, <https://doi.org/10.1021/cm3011474>.
- [42] R. B. Pujari, S. J. Patil, J. Park, A. Shanmugasundaram, D.-W. Lee, *J. Power Sources* **2019**, *436*, 226826, <https://doi.org/10.1016/j.jpowsour.2019.226826>.
- [43] L. Yang, S. Cheng, J. Wang, X. Ji, Y. Jiang, M. Yao, P. Wu, M. Wang, J. Zhou, M. Liu, *Nano Energy* **2016**, *30*, 293–302, <https://doi.org/10.1016/j.nanoen.2016.10.018>.
- [44] Q. Dou, Y. Lu, L. Su, X. Zhang, S. Lei, X. Bu, L. Liu, D. Xiao, J. Chen, S. Shi, *Energy Storage Mater.* **2019**, *23*, 603–609, <https://doi.org/10.1016/j.ensm.2019.03.016>.
- [45] Q. Xia, M. Xu, H. Xia, J. Xie, *ChemNanoMat* **2016**, *2*(7), 588–600, <https://doi.org/10.1002/cnma.20160110>.
- [46] P. Zhao, Q. Liu, X. Yang, J. Zhu, S. Yang, L. Chen, Q. Zhang, *J. Colloid Interface Sci.* **2024**, *662*, 322–332, <https://doi.org/10.1016/j.jcis.2024.02.039>.

Manuscript received: June 29, 2024

Revised manuscript received: September 26, 2024

Accepted manuscript online: October 8, 2024

Version of record online: November 12, 2024